Circulating Current Suppression of the Modular Multilevel Converter in a Double-Frequency Rotating Reference Frame

Behrooz Bahrani, *Member, IEEE*, Suman Debnath, *Student Member, IEEE*, and Maryam Saeedifard, *Senior Member, IEEE*

***Abstract*—The modular multilevel converter (MMC) has attracted significant interest for medium-/high-power energy conversion applications due to its modularity, scalability, and excellent harmonic performance. One of the technical challenges associated with the operation of the MMC is the circulation of double-frequency harmonic currents within its phase legs. This paper proposes a circulating current control strategy in a double-frequency rotating reference frame, which, contrary to the existing solutions that are based on approximate/inaccurate models, relies on an experimentally identified nonparametric model of circulating currents to determine the coefficients of the controller. Minimizing the squared second norm of the error between the open-loop transfer function of the system and a desired one, the coefficients of the controller are determined. To guarantee the stability of the closed-loop system, the minimization problem is subjected to a few constraints. The validity and effectiveness of the proposed control strategy is confirmed, and its dynamic performance is compared with that of an existing solution by experimental results.**

***Index Terms*—Circulating current, convex optimization, current control, double-frequency reference frame, loop shaping, modular multilevel converter (MMC).**

I. Introduction

THE modular multilevel converter (MMC) has become one of the most prominent converter topologies for medium/-high-power energy conversion applications, especially for high-voltage direct current transmission systems [1]–[9]. One of the main technical challenges associated with the operation of the MMC is the magnitude of the circulating currents within its phase legs [10], [11]. Circulating currents are dominantly negative-sequence second-order harmonic currents and do not impact the ac-side currents of the MMC. However, if not suppressed/controlled, circulating currents increase the rms values of the arm currents, leading to additional power losses and, especially at power factors close to unity, increased amplitude of submodule (SM) capacitor voltage ripple. Although proper sizing of the arm inductance can assist in reducing the magnitude of the circulating currents, an active circulating current control strategy is required to fully eliminate them. In the literature, various strategies have been proposed to suppress/regulate the circulating currents of the MMC [11]–[18]. Among the proposed strategies, proportional-resonant (PR) controllers tuned at the second harmonic [12] and proportional-integral (PI) controllers implemented in a double-frequency rotating reference frame [11] have become more popular due to their simplicity. However, these strategies tune the PR and PI controllers either heuristically or based on approximate/inaccurate models, which in any case are not necessarily optimal. Note that although the suppression of circulating currents is mainly the primary objective, in some applications, e.g., drive systems operating at low speed, circulating current controllers are utilized to inject specific circulating currents to reduce the magnitude of SM capacitor voltage ripple [19], [20].

In this paper, the nonparametric model of an experimental system representing the relationship between the control signals and the direct *(d)* and quadrature *(q)* components of the circulating currents in a double-frequency rotating reference frame is obtained. It is shown that this model is different from those used in the existing literature [11]. Based on the attained model, a 2×2 controller is designed that eliminates the *dq* components of the circulating currents in a double-frequency rotating reference frame. The 2×2 controller consists of four individual single-input single-output controllers. In contrast with the existing solutions, the proposed controller is designed through a loop-shaping technique, which adopts the nonparametric model of the system obtained through identification of the experimental system and, thus, does not rely on any inaccurate/approximate model. The performance of the proposed controller is experimentally evaluated and compared with that of the existing solution, and it is verified that the proposed controller results in superior dynamic performance.

The rest of this paper is structured as follows. In Section II, the study system is described, and an existing circulating current controller is detailed. In Section III, the nonparametric model of the system is derived, and based on that a 2×2 controller is designed through a loop-shaping technique. The performance of the designed controller based on experimental results is evaluated in Section IV. The conclusions are presented in Section V.

Manuscript received November 7, 2014; revised January 22, 2015; accepted February 5, 2015. Date of publication February 20, 2015; date of current version September 21, 2015. This work was supported by the Swiss National Science Foundation under Grant P2ELP2_149056 and also by the National Science Foundation under Grant 1102303. Recommended for publication by Associate Editor J. R. Rodriguez.

B. Bahrani and M. Saeedifard are with the School of Electrical and Computer Engineering, Georgia Institute of Technology, Atlanta, GA 30332 USA (e-mail: behrooz.bahrani@ece.gatech.edu; maryam@ece.gatech.edu).

S. Debnath is with the School of Electrical and Computer Engineering, Purdue University, West Lafayette, IN 47907 USA (e-mail: sdebnat@purdue.edu).

Color versions of one or more of the figures in this paper are available online at http://ieeexplore.ieee.org.

Digital Object Identifier 10.1109/TPEL.2015.2405062

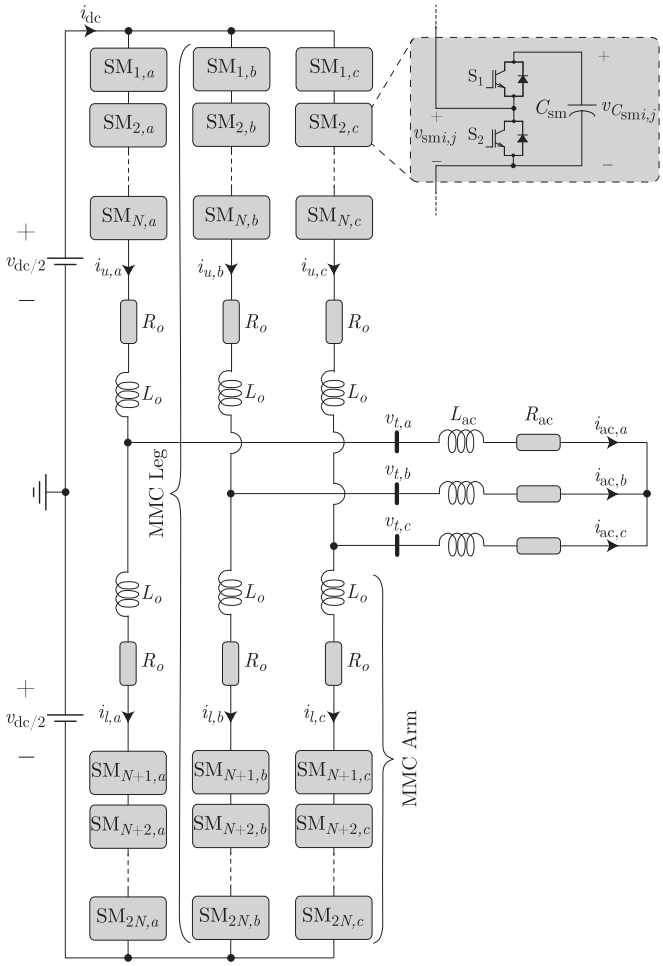

Fig. 1. Schematic diagram of a three-phase MMC.

II. Modular Multilevel Converter

A. Basics of Operation

A schematic diagram of the study system in which a three-phase RL load is fed by a three-phase MMC is shown in Fig. 1. The dc side of the MMC is supplied by a dc voltage source whose voltage is $v_{\rm dc}$. The three-phase MMC, as shown in Fig. 1, consists of three phases (legs), two arms per leg, i.e., an upper arm represented by subscript "u" and a lower arm represented by subscript "l". Each arm comprises N series-connected, nominally-identical half-bridge SMs, and a series inductor L_o. In addition, the resistor R_o represents the power losses within each arm of the converter. The arm inductors suppress high-frequency components in the arm currents, i.e., $i_{u,abc}$ and $i_{l,abc}$. Depending on the state of its two complementary switches, each SM of Fig. 1 can provide two voltage levels at its terminal, i.e., $v_{{\rm sm},i,j}=0$ or $v_{{\rm sm},i,j}=v_{C_{{\rm sm},i,j}}$. $v_{C_{{\rm sm},i,j}}$ is the capacitor voltage of the ith SM in the phase-leg j, where $i=1,2,\ldots,2N$; $j=a,b,c$. To determine the number of required SMs to be inserted in each arm, a distributed pulse width modulation (D-PWM) strategy is used in this paper [21].

Similar to any other multilevel converter topology, the MMC requires an active voltage balancing strategy to balance and maintain the SM capacitor voltages at $v_{\rm dc}/N$, where N is the number of SMs in each arm. To do so, a variation of the sorting algorithm is adopted in this paper [21]. The salient features of the SM capacitor voltage balancing strategy are lower switching frequency and computational burden, when compared to the existing SM capacitor voltage balancing strategies. This approach minimizes the switching frequency by allowing only one switch to change its state at any instant.

B. Circulating Current Control

In the MMC of Fig. 1, the upper and lower arm currents of the phase-j, $j=a,b,c$, i.e., $i_{u,j}$ and $i_{l,j}$, are expressed by

$$i_{u,j}=i_{{\rm diff},j}+\frac{i_{{\rm ac},j}}{2}\quad\text{and}\quad i_{l,j}=i_{{\rm diff},j}-\frac{i_{{\rm ac},j}}{2} \tag{1}$$

where $i_{{\rm diff},j}$ and $i_{{\rm ac},j}$ are the circulating current and the ac-side current in the phase-j, respectively. Therefore, the circulating current in the phase-j can be expressed by

$$i_{{\rm diff},j}=\frac{i_{u,j}+i_{l,j}}{2}. \tag{2}$$

Circulating currents do not impact the ac-side voltages $v_{t,abc}$ and currents $i_{{\rm ac},abc}$. However, if not properly controlled/suppressed, they result in excessive converter power losses, and increase the amplitude of the SM capacitor voltage ripple. In [22], the equation governing the circulating current dynamics in the phase-leg j is presented by

$$u_{{\rm diff},j}=L_o\frac{di_{{\rm diff},j}}{dt}+R_o i_{{\rm diff},j}=\frac{v_{\rm dc}}{2}-\frac{u_{u,j}+u_{l,j}}{2} \tag{3}$$

where $u_{{\rm diff},j}$ is the control signal used for controlling the circulating currents, and $u_{u,j}$ and $u_{l,j}$ are the sum of the inserted SM voltages of the upper and lower arm, respectively. Moreover, the emf generated by the phase-leg j is expressed by

$$e_j=\frac{u_{l,j}-u_{u,j}}{2} \tag{4}$$

which is used to control the ac-side currents. The reference signals for $u_{u,j}$ and $u_{l,j}$ are calculated such that both the ac side and circulating currents are regulated [11]. $u_{u,j,{\rm ref}}$ and $u_{l,j,{\rm ref}}$ are expressed by

$$u_{u,j,{\rm ref}}=\frac{v_{\rm dc}}{2}-e_j-u_{{\rm diff},j} \tag{5a}$$

$$u_{l,j,{\rm ref}}=\frac{v_{\rm dc}}{2}+e_j-u_{{\rm diff},j}. \tag{5b}$$

In (5), $u_{{\rm diff},j}$ regulates the circulating currents and does not affect e_j and, consequently, ac-side currents. e_j is dictated by other control loops responsible for power exchange or ac-side current regulation [23], [24]. The single-line diagram of the MMC-based system along with its controllers are shown in Fig. 2. Hereafter, as this paper is focused on the circulating current controller design, it is assumed that e_j, $j=a,b,c$, is given.

The circulating current flowing in each phase consists of a dc component and low-order harmonic components mainly with the frequency twice the fundamental one [25], [26]. Under balanced, steady-state conditions, the dc component is $i_{\rm dc}/3$, where

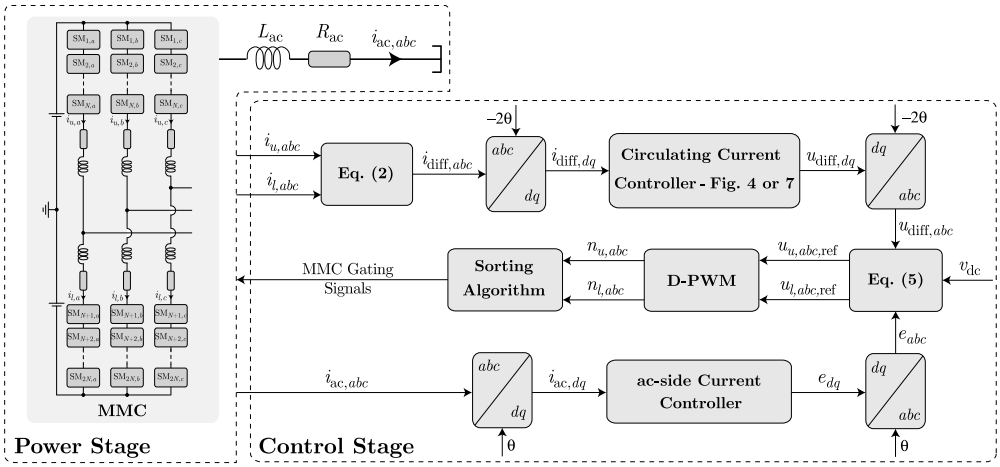

Fig. 2. Single-line diagram of the MMC-based system along with its controller.

$i_{\rm dc}$ is the dc-link current. Therefore, the circulating currents can be expressed by

$$i_{{\rm diff},a} = \frac{i_{\rm dc}}{3} + I_c \sin(2\omega_n t + \phi_0) \tag{6a}$$

$$i_{{\rm diff},b} = \frac{i_{\rm dc}}{3} + I_c \sin\left(2\omega_n t + \frac{2\pi}{3} + \phi_0\right) \tag{6b}$$

$$i_{{\rm diff},c} = \frac{i_{\rm dc}}{3} + I_c \sin\left(2\omega_n t - \frac{2\pi}{3} + \phi_0\right) \tag{6c}$$

where I_c is the amplitude of the circulating currents at twice the fundamental frequency [11]. The ac components of the circulating currents in (6) form a three-phase negative-sequence current. Applying Park transformation, the three-phase circulating currents are transformed to a double-frequency $dq0$ frame by

$$i_{{\rm diff},dq0} = \boldsymbol{T}_{abc,dq0} i_{{\rm diff},abc}. \tag{7}$$

The transformation matrix $\boldsymbol{T}_{abc,dq0}$ is

$$\boldsymbol{T}_{abc,dq0} = \frac{2}{3}\begin{bmatrix} \cos\theta_d & \cos(\theta_d - \frac{2\pi}{3}) & \cos(\theta_d + \frac{2\pi}{3}) \\ -\sin\theta_d & -\sin(\theta_d - \frac{2\pi}{3}) & -\sin(\theta_d + \frac{2\pi}{3}) \\ \frac{1}{2} & \frac{1}{2} & \frac{1}{2} \end{bmatrix} \tag{8}$$

where $\theta_d = \int^t -2\omega_n dt$, and ω_n is the angular frequency of the system. Transforming the mathematical equation given by (3) based on (8), the dynamic equation of circulating currents in a double-frequency rotating reference frame is expressed as

$$\begin{bmatrix} u_{{\rm diff},d} \\ u_{{\rm diff},q} \end{bmatrix} = L_o \frac{d}{dt}\begin{bmatrix} i_{{\rm diff},d} \\ i_{{\rm diff},q} \end{bmatrix} + \begin{bmatrix} 0 & -2\omega_n L_o \\ 2\omega_n L_o & 0 \end{bmatrix} \times \begin{bmatrix} i_{{\rm diff},d} \\ i_{{\rm diff},q} \end{bmatrix} + R_o \begin{bmatrix} i_{{\rm diff},d} \\ i_{{\rm diff},q} \end{bmatrix}. \tag{9}$$

Applying Laplace transform to (9), the system transfer functions from $u_{{\rm diff},dq}$ to $i_{{\rm diff},dq}$ are deduced and shown in Fig. 3. Based on these transfer functions, a circulating current controller in a double-frequency rotating reference frame is proposed in

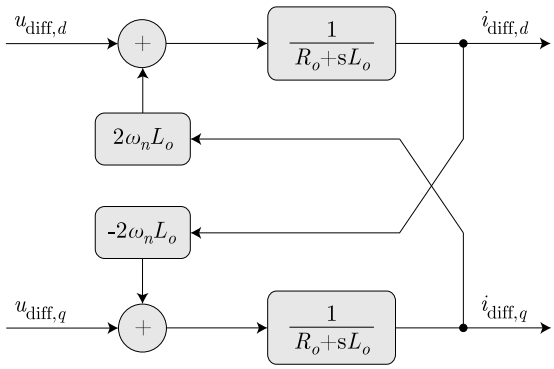

Fig. 3. System transfer function of the circulating currents.

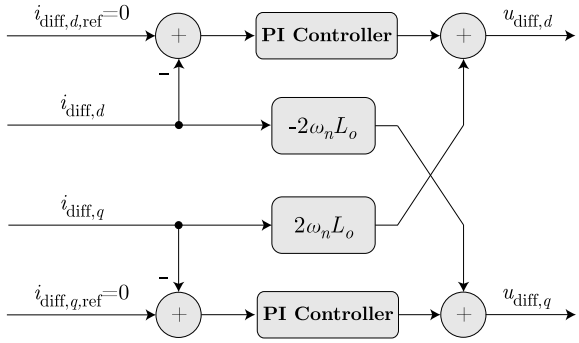

Fig. 4. The existing circulating current control strategy in [11].

[11], which is consisted of two PI controllers and two feed-forward terms. Assuming $i_{{\rm diff},dq,{\rm ref}} = 0$, the error signals in the d and q axes are generated and fed to the PI controllers. Furthermore, two feed-forward signals $2\omega_n L_o i_{{\rm diff},q}$ and $-2\omega_n L_o i_{{\rm diff},d}$ are added to the outputs of the PI controller in the d and q axes, respectively, which are to decouple the d and q components of the circulating currents. The structure of the controller is shown in Fig. 4. This control strategy relies on the developed model of (9), which is shown that is imprecise/inaccurate in this paper. Moreover, [11] does not discuss the details of determining the parameters of the PI controllers. In the following, relying on the nonparametric model of the system, which is identified by using

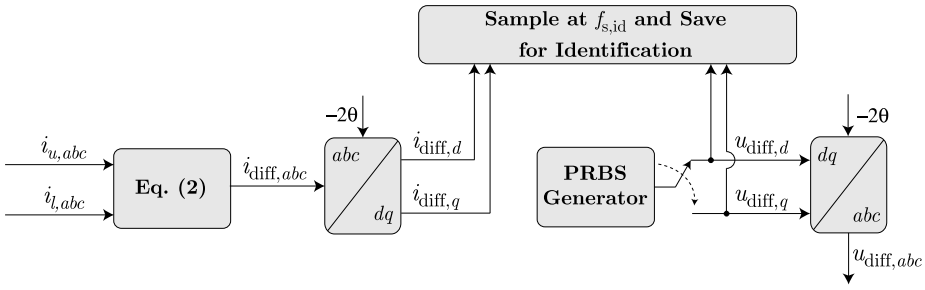

Fig. 5. Implementation block diagram of the identification that replaces the circulating current controller blocks of Fig. 2.

an experimental system, a 2×2 controller for suppressing the circulating currents is designed.

III. Proposed Circulating Current Controller

The proposed circulating current controller, similar to the controller of [11], has two inputs, i.e., the circulating current error signals in d and q axes, and two outputs, i.e., $u_{\rm diff,d}$ and $u_{\rm diff,q}$. However, the proposed one is consisted of four controllers, two in the direct axes and two in the transversal axes. In this section, the design procedure of this circulating current control strategy is detailed, which is based on a constrained optimization-based loop-shaping technique [27]. It uses the multi-input multi-output (MIMO) nonparametric model of the experimental MMC system of Fig. 1, i.e., $\boldsymbol{G}(j\omega)$, along with a linearly parameterized MIMO controller, i.e., $\boldsymbol{K}(z)$, to form an open-loop transfer function matrix, i.e., $\boldsymbol{L}(j\omega) = \boldsymbol{G}(j\omega)\boldsymbol{K}(j\omega) \forall \omega \in \mathbb{R}$. Based on the dynamic performance and the decoupling requirements, a desired open-loop transfer function matrix, i.e., $\boldsymbol{L}_{\rm D}(s)$, is also formed, and its diagonal and off-diagonal elements are determined. Minimizing the squared second norm of the error between the open-loop transfer function matrix and the desired one, the coefficients of the controller are optimally determined. To ensure the stability and the required dynamic performance of the closed-loop system, the minimization problem is subjected to a few constraints.

The design procedure is divided into three main steps [27]: 1) determination of the required nonparametric model, 2) determination of the class of the controller, and 3) solving the optimization problem and finding the optimal coefficients of the controller. In the following, these steps are detailed.

A. Nonparametric Model

To design the circulating current controller, the first step is to determine the nonparametric model of the system. The goal of a circulating current controller is to suppress the dq components of the circulating currents in the double-frequency rotating reference frame, i.e., $i_{{\rm diff},dq}$, by generating the dq components of the difference voltages, i.e., $u_{{\rm diff},dq}$. Therefore, the inputs of the to-be-controlled system are $u_{{\rm diff},dq}$, while its outputs are $i_{{\rm diff},dq}$. Thus, the system transfer function matrix is

$$\begin{bmatrix} i_{{\rm diff},d} \\ i_{{\rm diff},q} \end{bmatrix} = \underbrace{\begin{bmatrix} G_{11} & G_{12} \\ G_{21} & G_{22} \end{bmatrix}}_{\boldsymbol{G}} \begin{bmatrix} u_{{\rm diff},d} \\ u_{{\rm diff},q} \end{bmatrix}. \tag{10}$$

TABLE I
Parameters of the Study System of Fig. 1

Quantity	Value	Comment
L_o	2.2 mH	Arm Inductor
R_o	0.8 Ω	Resistor Representing Arm Loss
$C_{\rm sm}$	1.41 mF	SM Capacitance
$L_{\rm ac}$	1.1 mH	Load Inductance
$R_{\rm ac}$	8 Ω	Load Resistance
$S_{\rm base}$	2 kVA	MMC Rated Power
$v_{\rm dc}$	200 V	DC Bus Voltage
$f_{\rm sw}$	9 kHz	PWM Carrier Frequency
$f_{\rm s}$	9 kHz	Control Sampling Frequency
$f_{\rm s,id}$	3 kHz	Identification Sampling Frequency
f_n	60 Hz	System Nominal Frequency

To avoid any model approximation and simplification imposed by adopting the transfer function of Fig. 3, an accurate transfer function of the system is identified by utilizing an experimental MMC setup. To achieve the nonparametric model of the system of Fig. 1, $u_{{\rm diff},d}$ and $u_{{\rm diff},q}$ are separately excited with a stimulus signal, e.g., a pseudorandom binary sequence (PRBS) [28]. The PRBS is a periodic, deterministic sequence generated by a series of shift registers and Boolean algebra. The PRBS has three main design variables: 1) switching time, 2) number of shift registers or the PRBS order, and 3) the signal amplitude. The switching time is the amount of time between two PRBS elements, and it must be equal to the period of sampling for identification, i.e., $T_{\rm s,id} = \frac{1}{f_{\rm s,id}}$. In this paper, the PRBS order or the number of shift registers is chosen to be 10, which leads to a PRBS period of $(2^{10} - 1)T_{\rm s,id}$. Moreover, the PRBS amplitude must be large enough to excite the system; however, a very large amplitude may saturate and destabilize the system. In this paper, the amplitude of the PRBS for exciting $u_{{\rm diff},d}$ and $u_{{\rm diff},q}$ is selected at 0.02 p.u. Furthermore, the identification sampling frequency $f_{\rm s,id}$ may be different from the control sampling frequency $f_{\rm s}$, and in this paper, $f_{\rm s,id}$ is set at 3 kHz.

To obtain the transfer functions, the cross-correlation theorem is utilized [28]. Exciting the input u with a PRBS with the order of 10 for 2 periods, and saving the input u and output y at $f_{\rm s,id}$ for $2 \times 1023 \times T_{\rm s,id}$ s, the input autocorrelation, i.e., R_{uu}, and the input–output cross correlation, i.e., R_{uy} are calculated in discrete time. Then, the transfer function between the input and the output is calculated as

$$G(j\omega) = \frac{\mathscr{F}(R_{uy})}{\mathscr{F}(R_{uu})} \tag{11}$$

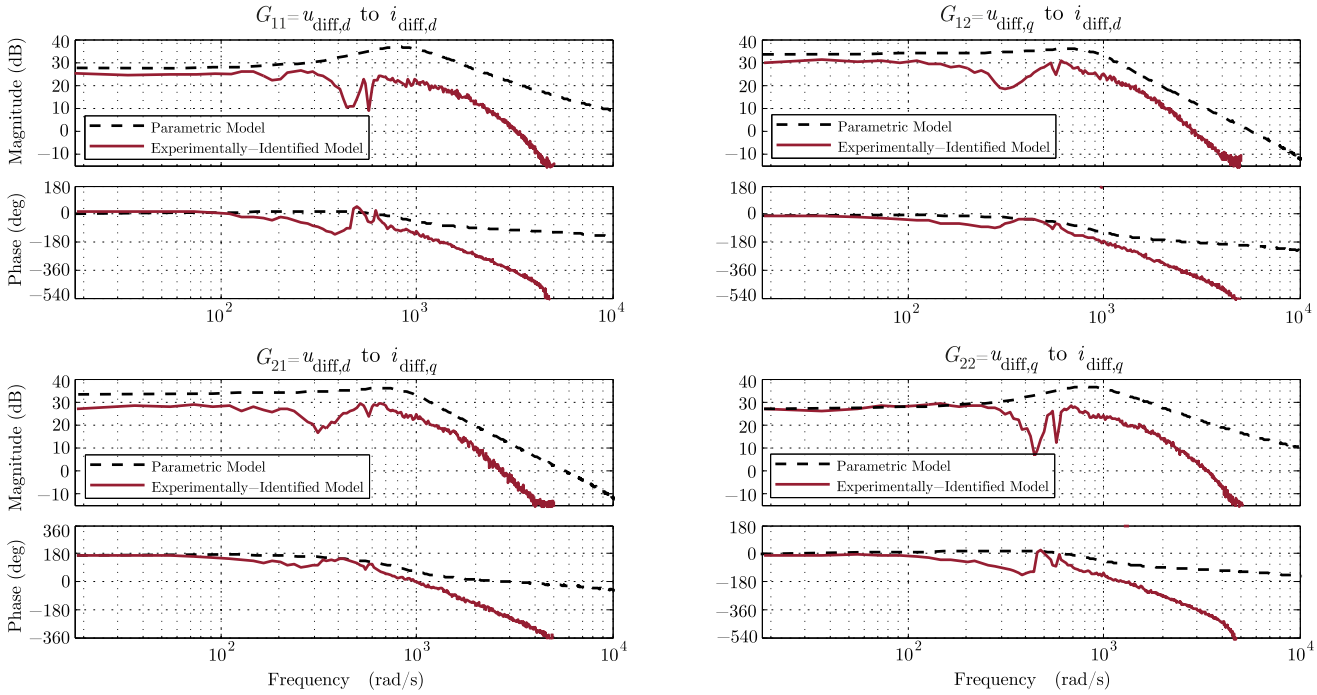

Fig. 6. Experimentally identified nonparametric model and the nonparametric model of the parametric transfer function of Fig. 3.

where ω belongs to a gridded linearly spaced interval from $\omega_{\min} = \frac{2\pi}{1023\times T_{\mathrm{s,id}}}$ to $\omega_{\max} = \frac{2\pi}{T_{\mathrm{s,id}}}$. To respect the Shanon theorem, the frequency points up to half of $\omega_{\max}$ are kept. Moreover, to reduce the effect of measurement errors and noise, instead of two, more periods of PRBS may be applied to the system, and the cross-correlation theorem may be applied over a large number of PRBS periods [28].

For the identification, no circulating current controller is in service and the inputs are separately excited. That is, initially, $u_{\mathrm{diff},q}$ is set to zero, and $u_{\mathrm{diff},d}$ is excited by the PRBS, and $u_{\mathrm{diff},dq}$ and $i_{\mathrm{diff},dq}$ are sampled at $f_{\mathrm{s,id}}$, which leads to the identification of G_{11} and G_{21}. The same holds for obtaining the nonparametric transfer functions between $u_{\mathrm{diff},q}$ and $i_{\mathrm{diff},dq}$, i.e., G_{22} and G_{12} through the excitation of $u_{\mathrm{diff},q}$. The implementation block diagram of the identification is illustrated in Fig. 5.

The experimentally identified nonparametric model corresponding to the experimental system of Fig. 1, whose parameters are listed in Table I, is depicted in Fig. 6. In addition, in Fig. 6, the nonparametric model of the system according to the derived transfer function of Fig. 3 is shown. The main distinction between the experimentally identified model and the model of Fig. 3 is that the experimentally identified one reflects the dynamics of the system without any approximation/simplification, especially at frequencies greater than 100 rad/s and, consequently, provides a more accurate model for control design purposes.

B. Controller Class

The proposed circulating current control strategy is responsible for suppressing the dq components of the circulating currents through manipulating the dq components of u_{diff}. Therefore, to control such a system, a 2×2 controller is required. A generic form of such a multivariable discrete-time controller in the z-domain is given by

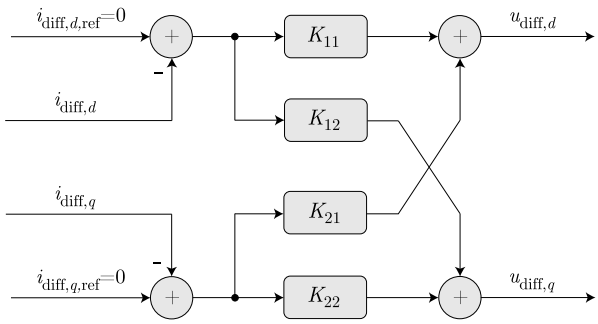

Fig. 7. Structural diagram of the proposed controller.

$$\begin{bmatrix} u_{\mathrm{diff},d} \\ u_{\mathrm{diff},q} \end{bmatrix} = \underbrace{\begin{bmatrix} K_{11} & K_{12} \\ K_{21} & K_{22} \end{bmatrix}}_{\boldsymbol{K}} \begin{bmatrix} e_{\mathrm{diff},d} \\ e_{\mathrm{diff},q} \end{bmatrix} \tag{12}$$

where $e_{\mathrm{diff},d}$ and $e_{\mathrm{diff},q}$ are the circulating current error signals in the d and q axes, respectively. The structural diagram of the controller is depicted in Fig. 7. Since the goal of the controller is to eliminate the steady-state error of $i_{\mathrm{diff},d}$ and $i_{\mathrm{diff},q}$, each element of the controller matrix, i.e., K_{xy}, $x = 1, 2$; $y = 1, 2$, comprises an integrator, which is represented by $\frac{1}{1-z^{-1}}$ in the discrete-time domain. Moreover, each element has two zeros in the z-domain. Therefore, each element of the controller matrix is equivalent to a PID-controller transformed to the z-domain via bilinear or Tustin transformation. For example, K_{11} is

given by

$$K_{11}(z,\boldsymbol{\rho}) = \frac{\rho_1 + \rho_2 z^{-1} + \rho_3 z^{-2}}{1 - z^{-1}} \tag{13}$$

in which the vector $\boldsymbol{\rho}$ contains the controller matrix coefficients as follows:

$$\boldsymbol{\rho} = [\rho_1, \rho_2, \ldots, \rho_{12}]. \tag{14}$$

The open-loop transfer function matrix of the system is then given by

$$\boldsymbol{L}(j\omega,\boldsymbol{\rho}) = \boldsymbol{G}(j\omega)\boldsymbol{K}(j\omega,\boldsymbol{\rho}) = \begin{bmatrix} L_{11} & L_{12} \\ L_{21} & L_{22} \end{bmatrix}. \tag{15}$$

It must be noted that PI controllers may also be utilized as the elements of the controller matrix. However, for this system, PID controllers result in better loop shaping and better dynamic performance.

C. Optimization-Based Loop Shaping

The loop shaping of the open-loop transfer function matrix, i.e., $\boldsymbol{L}$, is carried out by minimizing the squared second norm of the error between the individual entries of $\boldsymbol{L}$ and a desired open-loop transfer function matrix $\boldsymbol{L}_{\mathrm{D}}(s)$. Consequently, the control design procedure turns into an optimization problem as follows [27]:

$$\min_{\boldsymbol{\rho}} \parallel \boldsymbol{L}(\boldsymbol{\rho}) - \boldsymbol{L}_{\mathrm{D}} \parallel^2 . \tag{16}$$

The desired open-loop transfer function matrix $\boldsymbol{L}_{\mathrm{D}}$ is chosen to meet the system requirements, e.g., satisfactory dynamic response and reduced coupling between the outputs, i.e., $i_{\mathrm{diff},d}$ and $i_{\mathrm{diff},q}$. In this paper, the desired open-loop transfer function is selected as

$$\boldsymbol{L}_{\mathrm{D}}(s) = \begin{bmatrix} L_{\mathrm{D}1} & 0 \\ 0 & L_{\mathrm{D}2} \end{bmatrix} = \begin{bmatrix} \frac{\omega_c}{s} & 0 \\ 0 & \frac{\omega_c}{s} \end{bmatrix} \tag{17}$$

in which ω_c determines the bandwidth of the closed-loop system and is chosen $\omega_c = 250$ rad/s.

To ensure the stability and satisfactory dynamic performance of the to-be-designed controller, the minimization problem is subjected to several constraints. As proven in [27], to shape the sensitivity function of the closed-loop system, the minimization problem must be subjected to the following linear constraints:

$$\begin{aligned} &|W_1(j\omega)[1 + L_{\mathrm{D}p}(j\omega,\boldsymbol{\rho})]| - \\ &\mathcal{R}e\{[1 + L_{\mathrm{D}p}(-j\omega)][1 + L_{pp}(j\omega,\boldsymbol{\rho})]\} < 0 \\ &\forall\omega \in \mathbb{R} \text{ and } p = 1,2 \end{aligned} \tag{18}$$

where $W_1(j\omega)$ is a weighting filter. In this paper, $W_1(j\omega) = 0.5$, which guarantees a gain margin of at least 2 and a phase margin of greater than 29° [29]. Moreover, to ensure the stability of the closed-loop system, the minimization problem must satisfy the generalized Nyquist stability criterion. Therefore, as proved in [27], the minimization problem must also satisfy the following constraints:

$$\begin{aligned} &r_p(\omega,\boldsymbol{\rho}) - \frac{\mathcal{R}e\{[1 + L_{\mathrm{D}p}(-j\omega)][1 + L_{pp}(j\omega,\boldsymbol{\rho})]\}}{|1 + L_{\mathrm{D}p}(j\omega)|} < 0 \\ &\forall\omega \in \mathbb{R} \text{ and } p = 1,2 \end{aligned} \tag{19}$$

where $r_1(\omega,\boldsymbol{\rho})$ and $r_2(\omega,\boldsymbol{\rho})$ are defined as

$$r_1(\omega,\boldsymbol{\rho}) = |L_{21}(j\omega,\boldsymbol{\rho})| \text{ and } r_2(\omega,\boldsymbol{\rho}) = |L_{12}(j\omega,\boldsymbol{\rho})|. \tag{20}$$

The optimization problem of (16) constrained to (18) and (19), known as a semi-infinite problem (SIP), includes infinite number of constraints and finite number of variables. A practical solution to this problem is to neglect the frequencies above a certain frequency, i.e., $\omega_{\max}$, for which the gains of the elements of the open-loop transfer function matrix are close to zero. In discrete-time systems, the frequencies above the Nyquist frequency can be neglected. Moreover, to have a finite number of frequency points, the gridded frequency interval $[0\ \omega_{\max}]$ can be taken, which contains finite frequency points. Therefore, the SIP problem turns into a semidefinite problem (SDP) and can be solved utilizing the standard SDP solvers, e.g., SeDuMi [30].

Choosing M linearly spaced frequencies within the range of $[0\ \omega_{\max}] \in \mathbb{R}$, the quadratic objective function is approximated by

$$\parallel \boldsymbol{L}(\boldsymbol{\rho}) - \boldsymbol{L}_{\mathrm{D}} \parallel^2 \approx \sum_{k=1}^{M} \parallel \boldsymbol{L}(j\omega_k,\boldsymbol{\rho}) - \boldsymbol{L}_{\mathrm{D}}(j\omega_k) \parallel_F \tag{21}$$

where $\|.\|_F$ is the Frobenius norm [27]. Therefore, the following optimization problem is deduced:

$$\min_{\boldsymbol{\rho}} \sum_{k=1}^{M} \parallel \boldsymbol{L}(j\omega_k,\boldsymbol{\rho}) - \boldsymbol{L}_{\mathrm{D}}(j\omega_k) \parallel_F \tag{22}$$

subjected to

$$\begin{aligned} &|W_1(j\omega_k)[1 + L_{\mathrm{D}p}(j\omega_k)]| \\ &- \mathcal{R}e[1 + L_{\mathrm{D}p}(-j\omega_k)][1 + L_{pp}(j\omega_k,\boldsymbol{\rho})] < 0 \\ &\text{for } k = 1,\ldots,M \text{ and } p = 1,2 \end{aligned}$$

and

$$\begin{aligned} &r_p(\omega_k,\boldsymbol{\rho}) - \frac{\mathcal{R}e\{[1 + L_{\mathrm{D}p}(-j\omega_k)][1 + L_{pp}(j\omega_k,\boldsymbol{\rho})]\}}{|1 + L_{\mathrm{D}p}(j\omega_k)|} < 0 \\ &\text{for } k = 1,\ldots,M, \text{ and } p = 1,2. \end{aligned}$$

Solving the minimization problem of (22) for the experimentally identified nonparametric model, the controller matrix is

$$\boldsymbol{K}(z) = \begin{bmatrix} \dfrac{0.1135 - 0.2174z^{-1} + 0.1043z^{-2}}{1 - z^{-1}} & \dfrac{0.0091 - 0.0075z^{-1} - 0.0011z^{-2}}{1 - z^{-1}} \\ \dfrac{-0.0429 + 0.0746z^{-1} - 0.0322z^{-2}}{1 - z^{-1}} & \dfrac{0.1027 - 0.1981z^{-1} + 0.0957z^{-2}}{1 - z^{-1}} \end{bmatrix}. \tag{23}$$

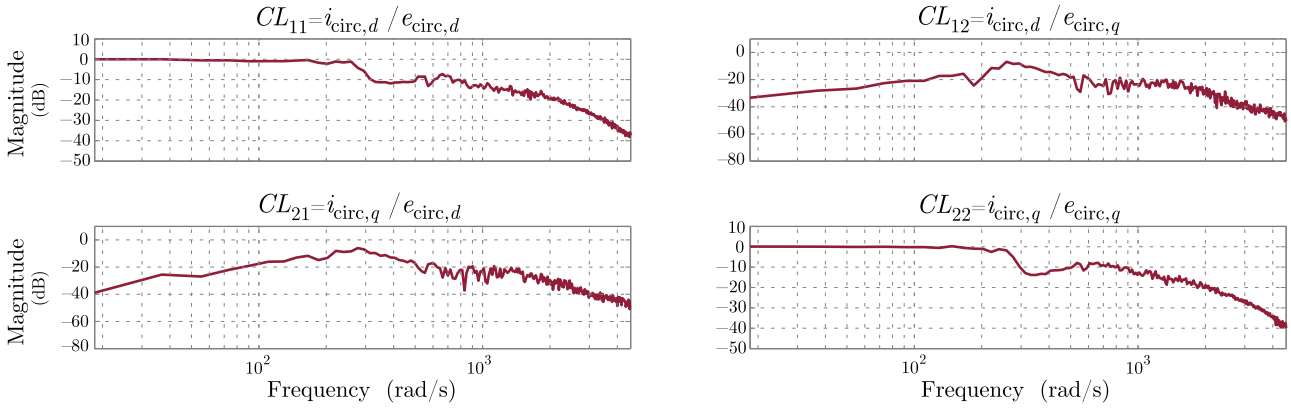

Fig. 8. Frequency response of the closed-loop transfer function matrix of the system of Fig. 2.

calculated and represented by (23) is shown at the bottom of the previous page.

Upon obtaining the frequency response of the designed controller, the frequency response of the open-loop transfer function matrix can be obtained as $\boldsymbol{L}(j\omega) = \boldsymbol{G}(j\omega)\boldsymbol{K}(j\omega)\forall\omega \in \mathbb{R}$. Subsequently, the frequency response of the closed-loop system is obtained by

$$\boldsymbol{CL}(j\omega) = \begin{bmatrix} \boldsymbol{CL}_{11} & \boldsymbol{CL}_{12} \\ \boldsymbol{CL}_{21} & \boldsymbol{CL}_{22} \end{bmatrix} = \frac{\boldsymbol{L}(j\omega)}{1+\boldsymbol{L}(j\omega)}\forall\omega \in \mathbb{R}. \quad (24)$$

The frequency response of the closed-loop system of the circulating current controller with a bandwidth of 250 rad/s for the diagonal elements of $\boldsymbol{CL}$ is depicted in Fig. 8. Moreover, in Fig. 8, the gains of the off-diagonal elements of $\boldsymbol{CL}$, i.e., $\boldsymbol{CL}_{12}$ and $\boldsymbol{CL}_{21}$, are very low, which confirms the d and q axes are well decoupled.

IV. Performance Evaluation

In this section, the performance of the proposed circulating current controller is experimentally evaluated on a five-level MMC prototype. The controllers are implemented using an Opal-RT real-time simulator. Four testing scenarios are conducted: 1) steady-state operation of the MMC system without any circulating current controller, 2) steady-state operation of the system with the proposed circulating current controller, 3) dynamic response of the circulating current controller upon a step-up change in e_q, and 4) dynamic response of the controller upon a step-down change in e_q. Moreover, the dynamic performance of the proposed controller is experimentally compared with that of the existing approach of [11].

A. Steady-State Operation of the Proposed Controller

To show the effectiveness and performance of the proposed circulating current controller, two tests under steady-state conditions are conducted, and the results are shown in Figs. 9 and 10. In the first test, no circulating current controller is utilized, and the system is operating in the steady state. The reference values for the MMC ac-side terminal voltages in the rotating reference frame are $e_d = 0$ V and $e_q = 85$ V. The rest of the

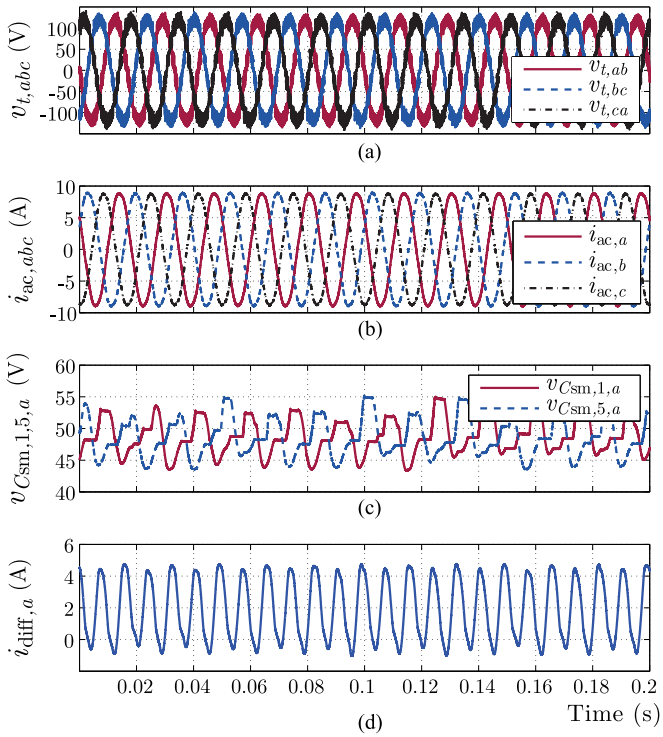

Fig. 9. Steady-state waveforms of the MMC with no circulating current controller: (a) three-phase ac-side phase voltages, (b) three-phase ac-side currents, (c) SM capacitor voltages in the upper and lower arms of phase-a $v_{C_{\mathrm{sm},1,a}}$ and $v_{C_{\mathrm{sm},5,a}}$, and (d) phase-a circulating current.

system parameters are set based on the parameters in Table I. The three-phase line-to-line voltages are shown in Fig. 9(a) whose amplitudes are fixed as their reference signals in the rotating reference frame are fixed. The ac-side currents are illustrated in Fig. 9(b). The amplitude of the ac-side currents are also fixed since $v_{t,abc}$ and the load parameters are unchanged. The SM capacitor voltage of two SMs of the phase-a, one in the upper arm and one in the lower arm, are shown in Fig. 9(c). As shown, the SM capacitor voltages are maintained at $v_{\mathrm{dc}}/4 = 50$ V and are balanced by the balancing strategy. The circulating current in the phase-a is depicted in Fig. 9(d), which contains a dc component, i.e., one-third of the dc-link current, and an ac component

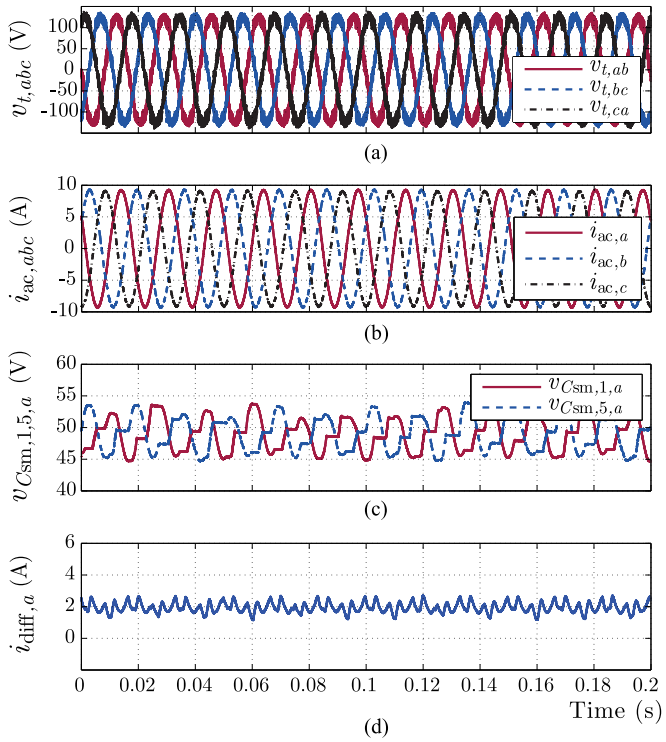

Fig. 10. Steady-state waveforms of the MMC, while the circulating current controller is in service: (a) three-phase ac-side phase voltages, (b) three-phase ac-side currents, (c) SM capacitor voltages in the upper and lower arms of phase-a $v_{C_{\mathrm{sm},1,a}}$, and $v_{C_{\mathrm{sm},5,a}}$ and (d) phase-a circulating current.

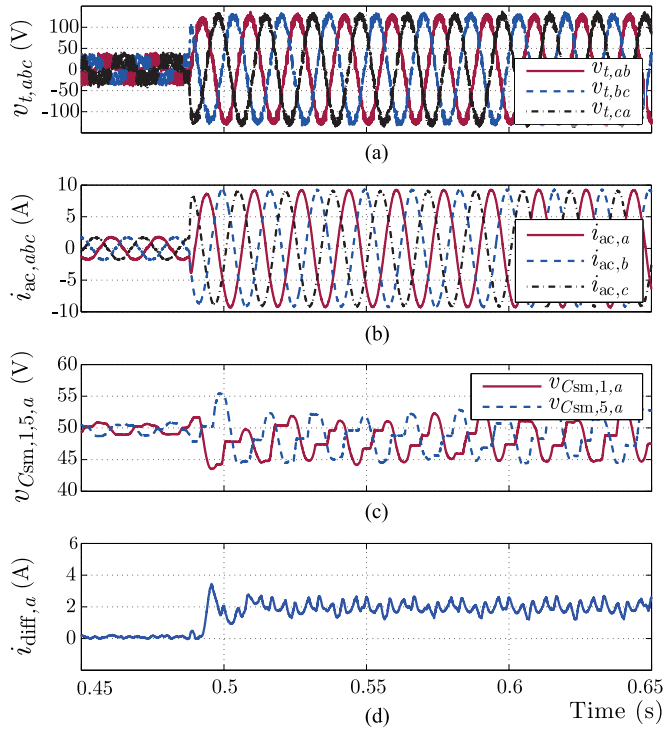

Fig. 11. Dynamic response of the proposed controller to a step-up change in e_q: (a) MMC ac-side phase voltages, (b) ac-side currents, (c) SM capacitor voltages in the upper and lower arms of phase-a $v_{C_{\mathrm{sm},1,a}}$ and $v_{C_{\mathrm{sm},5,a}}$, and (d) phase-a circulating current.

at double-frequency. The amplitude of the ac component is comparable to the dc component, and if not suppressed, results in excessive SM capacitor voltage ripple and loss.

The dual of the waveforms of Fig. 9, while the proposed circulating current controller is in service are depicted in Fig. 10. As expected and shown in Figs. 10(a) and (b), the ac-side terminal voltages and currents remain unchanged and identical to those of the previous test scenario. Two of the SM capacitor voltages are shown in Fig. 10(c), and the circulating current in the phase-a is illustrated in Fig. 10(d). Since the proposed circulating current controller is active and suppresses the double-frequency component of the circulating currents, the amplitude of the SM capacitor voltage ripple compared to the previous case becomes smaller. The circulating current, which does not include any double-frequency component, only contains a dc component and higher order harmonic components, e.g., fourth-order harmonic component.

B. Dynamic Response of the Proposed Controller

To evaluate the dynamic performance of the proposed circulating current controller upon changes in the ac-side variables, two tests are conducted in this section. The experimental setup is initially operating in steady state. The reference signals of $v_{t,abc}$ in dq frame, i.e., e_{dq}, are changed, and the proposed controller is expected to suppress the double-frequency component of the circulating currents, prior to and subsequent to the changes.

In the first test, the q component of the reference signal of the ac-side terminal voltages, i.e., e_q, is stepped up from 20 to 85 V, at $t = 0.487$ s, while all other parameters are kept constant. As illustrated in Fig. 11(a), the ac-side terminal voltages of the MMC are stepped up subsequent to the change in their reference signals. Moreover, the load currents follow the same pattern as the voltages, as shown in Fig. 11(b). The capacitor voltages of two SMs, one in the upper and one in the lower arm of the phase-a, are shown in Fig. 11(c). Prior to the step-up change, the capacitor voltages are balanced at 50 V and have a ripple component of almost 2 V. Subsequent to the change, the capacitor voltages are still balanced by the balancing strategy. However, their ripple component is increased to almost 4 V as the amplitude of the arm currents also increases. The circulating current in the phase-a is depicted in Fig. 11(d), which prior to the change has a dc component, as well as negligible high-order harmonic components. Upon the change, the proposed circulating current controller, after a transient period of less than 10 ms, suppresses the double-frequency component of the circulating current, which is compatible with the predicted closed-loop bandwidth of the designed controller. However, in the steady state, the circulating current contains fourth-order harmonic components.

The dual waveforms of Figs. 11 for a step down change in e_q are depicted in Fig. 12. At $t = 0.512$ s, e_q is stepped down from 85 to 20 V. The ac-side variables, i.e., $v_{t,abc}$ and $i_{\mathrm{ac},abc}$ as illustrated in Figs. 12(a) and (b), follow the same pattern, and are stepped down subsequent to the change in e_q. Moreover, subsequent to the step-down change, since less current flows in each arm, the amplitude of the SM capacitor voltage ripple

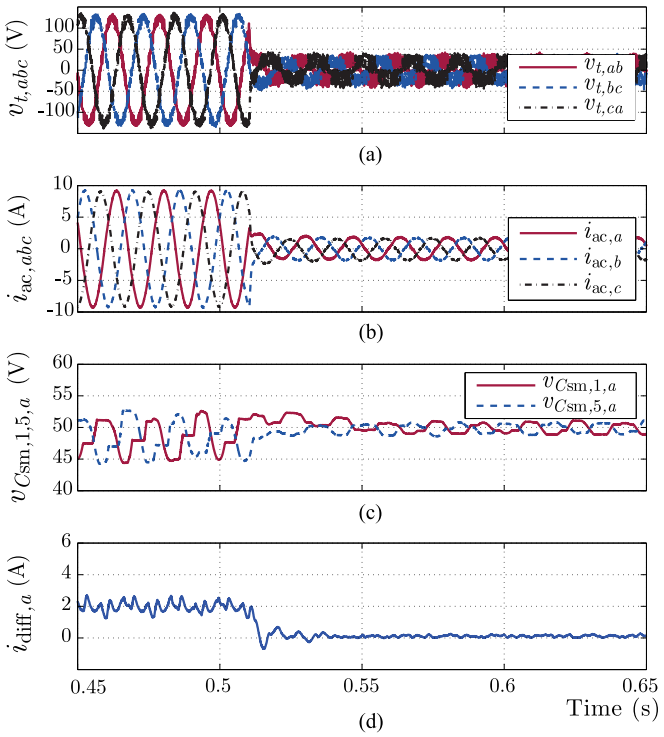

Fig. 12. Dynamic response of the proposed controller to a step-down change in e_q: (a) MMC ac-side phase voltages, (b) ac-side currents, (c) SM capacitor voltages in the upper and lower arms of phase-a $v_{C_{\mathrm{sm},1,a}}$ and $v_{C_{\mathrm{sm},5,a}}$, and (d) phase-a circulating current.

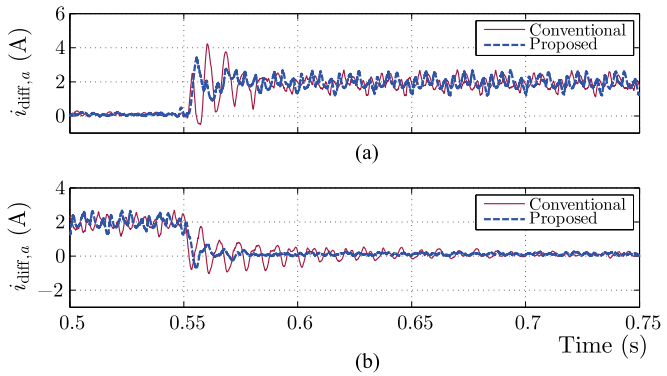

Fig. 13. Dynamic performance of the proposed controller and the controller of [11] subsequent to changes in e_q: (a) phase-a circulating current during a step-up change in e_q, and (b) phase-a circulating current during a step-down change in e_q.

decreases, as shown in Fig. 12(c). The phase-a circulating current is depicted in Fig. 12(d), which prior to and subsequent to the step-down change, does not contain double-frequency harmonic component. As shown in Fig. 12(d), upon the change of e_q, the circulating current controller suppresses the double-frequency component in less than 10 ms.

C. Dynamic Response Comparison With the Existing Solution

To compare the dynamic performance of the proposed controller with the conventional approach of [11], the controller structure of Fig. 4 is taken, and the required PI controllers are designed. To tune the parameters of the PI controllers, a zero-pole cancellation approach is adopted. Thus, the pole of the system, i.e., $s = -\frac{R_o}{L_o}$ is cancelled by the zero of the PI controller. Therefore, the PI controllers of Fig. 4 are $K_{\mathrm{PI}} = K_p \frac{L_o s + R_o}{s}$. Consequently, the diagonal elements of the open-loop transfer function matrix of the system, assuming the model of Fig. 3 is accurate, becomes $L_{ii} = G_{ii} K_{\mathrm{PI}} = \frac{1}{L_o s + R_o} K_p \frac{L_o s + R_o}{s} = \frac{K_p}{s}$, where K_p is determined based on the required bandwidth of the closed-loop system, and $i = 1, 2$. In this test, the bandwidth of the closed-loop system for the conventional approach of [11] is chosen to be 250 rad/s, which is similar to the bandwidth of the system with the designed controller in Section III.

For the comparison, the dual of the tests performed in Section IV-B are repeated, while the controller of [11] is in service. The experimental setup is initially operating in steady state. At $t = 0.55$ s, a step change is imposed on e_q. In Fig. 13(a), the circulating current in phase-a is shown prior and, subsequent, to a step-up change in e_q from 20 to 85 V for both controllers. The step-down test results are also shown in Fig. 13(b), where e_q is stepped down from 85 to 20 V. The proposed controller suppresses the second-harmonic oscillation in less than a cycle, while the controller of [11] needs several cycles to reach steady state. Moreover, the overshoot of the circulating current subsequent to transients for the controller of [11] is almost twice as that of the proposed controller.

V. Conclusion

In this paper, a circulating current control strategy in a double-frequency rotating reference frame for the MMC is proposed. Contrary to the existing circulating current controllers, the proposed approach does not rely on any mathematical approximate/inaccurate model to design the controller. Instead, it takes an experimentally identified nonparametric model of the system to design the controller. Taking the experimentally identified model, a 2×2 controller is designed, whose design procedure is based on loop shaping and involves three main steps: 1) attaining an experimentally identified nonparametric model of the system, 2) determining the class of the to-be-designed controller, and 3) solving a constrained convex optimization problem. The performance of the proposed controller is experimentally evaluated under several operating scenarios. The experimental results confirm the superior dynamic performance of the proposed control strategy in terms of suppressing the circulating currents compared to the existing solution.

References

[1] R. Marquardt, "Modular multilevel converter: An universal concept for HVDC-networks and extended DC-bus-applications," in *Proc. Int. Power Electron. Conf.*, Jun. 2010, pp. 502–507.

[2] M. Guan and Z. Xu, "Modeling and control of a modular multilevel converter-based HVDC system under unbalanced grid conditions," *IEEE Trans. Power Electron.*, vol. 27, no. 12, pp. 4858–4867, Dec. 2012.

[3] J. Peralta, H. Saad, S. Dennetiere, J. Mahseredjian, and S. Nguefeu, "Detailed and averaged models for a 401 level MMC HVDC system," *IEEE Trans. Power Del.*, vol. 27, no. 3, pp. 1501–1508, Jul. 2012.

[4] J. Qin and M. Saeedifard, "Predictive control of a modular multilevel converter for a back-to-back HVDC system," *IEEE Trans. Power Del.*, vol. 27, no. 3, pp. 1538–1547, Jul. 2012.
[5] K. Sekiguchi, P. Khamphakdi, M. Hagiwara, and H. Akagi, "A grid-level high-power BTB (back-to-back) system using modular multilevel cascade converters without common DC-link capacitor," *IEEE Trans. Ind. Appl.*, vol. 50, no. 4, pp. 2648–2659, Jul. 2014.
[6] M. Saeedifard and R. Iravani, "Dynamic performance of a modular multilevel back-to-back HVDC system," *IEEE Trans. Power Del.*, vol. 25, no. 4, pp. 2903–2912, Oct. 2010.
[7] S. Debnath, J. Qin, B. Bahrani, M. Saeedifard, and P. Barbosa, "Operation, control, and applications of the modular multilevel converter: A review," *IEEE Trans. Power Electron.*, vol. 30, no. 1, pp. 37–53, Jan. 2015.
[8] G. Bergna, E. Berne, P. Egrot, P. Lefranc, A. Arzande, J.-C. Vannier, and M. Molinas, "An energy-based controller for HVDC modular multilevel converter in decoupled double synchronous reference frame for voltage oscillation reduction," *IEEE Trans. Ind. Electron.*, vol. 60, no. 6, pp. 2360–2371, Jun. 2013.
[9] E. Solas, G. Abad, J. Barrena, S. Aurtenetxea, A. Carcar, and L. Zajac, "Modular multilevel converter with different submodule concepts—Part II: Experimental validation and comparison for HVDC application," *IEEE Trans. Ind. Electron.*, vol. 60, no. 10, pp. 4536–4545, Oct. 2013.
[10] J. Pou, S. Ceballos, G. Konstantinou, V. Agelidis, R. Picas, and J. Zaragoza, "Circulating current injection methods based on instantaneous information for the modular multilevel converter," *IEEE Trans. Ind. Electron.*, vol. 62, no. 2, pp. 777–788, Feb. 2015.
[11] Q. Tu, Z. Xu, and L. Xu, "Reduced switching-frequency modulation and circulating current suppression for modular multilevel converters," *IEEE Trans. Power Del.*, vol. 26, no. 3, pp. 2009–2017, Jul. 2011.
[12] S. Debnath and M. Saeedifard, "A new hybrid modular multilevel converter for grid connection of large wind turbines," *IEEE Trans. Sustainable Energy*, vol. 4, no. 4, pp. 1051–1064, Oct. 2013.
[13] L. Harnefors, A. Antonopoulos, S. Norrga, L. Angquist, and H.-P. Nee, "Dynamic analysis of modular multilevel converters," *IEEE Trans. Ind. Electron.*, vol. 60, no. 7, pp. 2526–2537, Jul. 2013.
[14] X. She, A. Huang, X. Ni, and R. Burgos, "AC circulating currents suppression in modular multilevel converter," in *Proc. IEEE 38th Annu. Conf. Ind. Electron. Soc.*, Oct. 2012, pp. 191–196.
[15] M. Vasiladiotis, N. Cherix, and A. Rufer, "Accurate capacitor voltage ripple estimation and current control considerations for grid-connected modular multilevel converters," *IEEE Trans. Power Electron.*, vol. 29, no. 9, pp. 4568–4579, Sep. 2014.
[16] L. He, K. Zhang, J. Xiong, and S. Fan, "Repetitive control scheme for circulating current suppression in modular multilevel converters," in *Proc. IEEE Energy Convers. Congr. Expo.*, Sep. 2013, pp. 963–969.
[17] G. Bergna, J.-A. Suul, E. Berne, J.-C. Vannier, and M. Molinas, "MMC circulating current reference calculation in ABC frame by means of lagrange multipliers for ensuring constant DC power under unbalanced grid conditions," in *Proc. 16th Eur. Conf. Power Electron. Appl.*, Aug. 2014, pp. 1–10.
[18] G. Bergna, A. Garces, E. Berne, P. Egrot, A. Arzande, J.-C. Vannier, and M. Molinas, "A generalized power control approach in ABC frame for modular multilevel converter HVDC links based on mathematical optimization," *IEEE Trans. Power Del.*, vol. 29, no. 1, pp. 386–394, Feb. 2014.
[19] S. Engel and R. De Doncker, "Control of the modular multi-level converter for minimized cell capacitance," in *Proc. 14th Eur. Conf. Power Electron. Appl.,* Aug. 2011, pp. 1–10.
[20] M. Winkelnkemper, A. Korn, and P. Steimer, "A modular direct converter for transformerless rail interties," in *Proc. IEEE Int. Symp. Ind. Electron.*, Jul. 2010, pp. 562–567.
[21] S. Debnath, J. Qin, and M. Saeedifard, "A distributed PWM strategy for modular multilevel converter," presented at 40th Annu. Conf. IEEE Industrial Electronics Society, Oct. 29 2014–Nov. 1 2014, pp. 1014–1020.
[22] A. Antonopoulos, L. Angquist, and H.-P. Nee, "On dynamics and voltage control of the modular multilevel converter," in *Proc. 13th Eur. Conf. Power Electron. Appl.*, Sep. 2009, pp. 1–10.
[23] B. Bahrani, A. Karimi, B. Rey, and A. Rufer, "Decoupled dq-current control of grid-tied voltage source converters using nonparametric models," *IEEE Trans. Ind. Electron.*, vol. 60, no. 4, pp. 1356–1366, Apr. 2013.
[24] B. Bahrani, S. Kenzelmann, and A. Rufer, "Multivariable-PI-based dq Current control of voltage source converters with superior axis decoupling capability," *IEEE Trans. Ind. Electron.*, vol. 58, no. 7, pp. 3016–3026, Jul. 2011.
[25] S. Rohner, S. Bernet, M. Hiller, and R. Sommer, "Modelling, simulation and analysis of a modular multilevel converter for medium voltage applications," in *Proc. IEEE Int. Conf. Ind. Technol.*, Mar. 2010, pp. 775–782.
[26] Q. Tu, Z. Xu, H. Huang, and J. Zhang, "Parameter design principle of the arm inductor in modular multilevel converter based HVDC," in *Proc. Int. Conf. Power Sys. Technol.*, Oct. 2010, pp. 1–6.
[27] G. Galdos, A. Karimi, and R. Longchamp, "H∞ controller design for spectral MIMO models by convex optimization," *J. Process Control*, vol. 20, no. 10, pp. 1175–1182, 2010.
[28] T. Söderström and P. Stoica, *System Identification*. Englewood Cliffs, NJ, USA: Prentice-Hall, 1989.
[29] I. D. Landau, R. Lozano, M. M'Saad, and A. Karimi, *Adaptive Control, Algorithms, Analysis and Applications*. New York, NY, USA: Springer-Verlag, USA, 2011.
[30] J. F. Strum, "Using SeDuMi 1.02, a Matlab toolbox for optimization over symmetric cones," in *Proc. Optim. Methods Softw.*, vol. 11, 1999, pp. 625–653.

Behrooz Bahrani (S'07–M'12) received the B.Sc. degree from the Sharif University of Technology, Tehran, Iran, the M.Sc. degree from the University of Toronto, Toronto, ON, Canada, and the Ph.D. degree from Ecole Polytechnique Fédérale de Lausanne, Lausanne, Switzerland, in 2006, 2008, and 2012, respectively, all in electrical engineering.

He is currently a Postdoctoral Fellow at the Georgia Institute of Technology, Atlanta, GA, USA. His research interests include control of power electronic systems, applications of power electronics in power and traction systems, and grid integration of renewable energy resources.

Suman Debnath (S'13) was born in Thiruvananthapuram, India, in 1988. He received the B.S. and M.S. degrees in electrical engineering from the Indian Institute of Technology Madras, Madras, TN, India, in 2010. Since 2010, he has been working toward the Ph.D. degree at the Power and Energy Devices and Systems Group, Purdue University, West Lafayette, IN, USA.

His main research interest includes power electronics and its applications.

Maryam Saeedifard (SM'11) received the Ph.D. degree in electrical engineering from the University of Toronto, Toronto, ON, Canada, in 2008.

She was an Assistant Professor with the School of Electrical and Computer Engineering, Purdue University, West Lafayette, IN, USA, prior joining Georgia Tech. She is currently as Assistant Professor at the School of Electrical and Computer Engineering, Georgia Institute of Technology, Atlanta, GA, USA. Her research interests include power electronics and applications of power electronics in power systems.